ACS APPLIED POLYMER MATERIALS

pubs.acs.org/acsapm
Article

Hybrid Porous Polymers Combination of Octavinylsilsesquioxane/Pyrene with Benzothiadiazole Units for Robust Energy Storage and Efficient Photocatalytic Hydrogen Production from Water

Mohamed Gamal Mohamed,* Mohamed Hammad Elsayed,* Ahmed E. Hassan, Abdul Basit, Islam M. A. Mekhemer, Ho-Hsiu Chou, Kuei-Hsien Chen, and Shiao-Wei Kuo*

Cite This: *ACS Appl. Polym. Mater.* 2024, 6, 5945−5956

Read Online

ACCESS | Metrics & More | Article Recommendations | Supporting Information

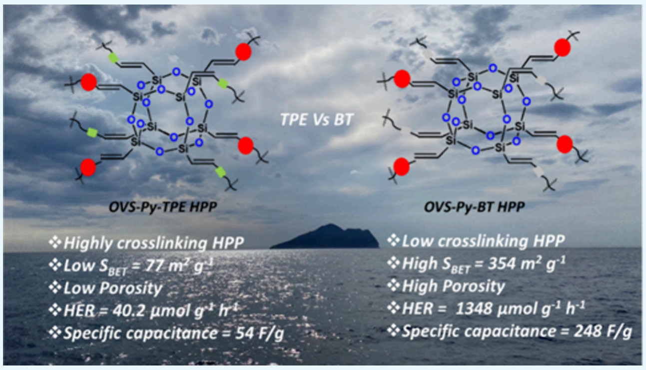

ABSTRACT: We investigated the performance that is improved in various applications through molecular structural alterations. Specifically, we emphasized the importance of controlling the branching densities of organic moieties as a useful tactic for varying the surface area and porosity of hybrid porous organic/inorganic polymers (HPPs), which include octavinylsilsesquioxane (OVS) units. This study shows that adjusting the branching densities could greatly enhance energy storage and hydrogen production. The two-branched chemical structure (4,7-dibromo-2,1,3-benzothiadiazole, BT-Br_2) and the four-branched organic compound (1,1,2,2-tetrakis(4-bromophenyl)ethylene, TPE-Br_4) are individually reacted with OVS and 1,3,6,8-tetrabromopyrene (Py-Br_4) twice to prepare the HPPs. These materials with high or low cross-linking density, as well as small and large surface areas, are synthesized by this dual reaction, which also produces HPPs with different cross-linking densities. Based on Brunauer−Emmett−Teller calculations, the OVS-Py-BT HPP has more than 4.5 times larger surface area than the OVS-Py-TPE HPP material. Remarkably, OVS-Py-BT HPP exhibited exceptional results for supercapacitor applications, with specific capacitance values of 248 and 54 F/g for OVS-Py-BT and OVS-Py-TPE HPPs, respectively, as determined by galvanostatic charge−discharge. OVS-Py-BT HPP significantly outperformed OVS-Py-TPE HPP in photocatalytic hydrogen evolution. This is evident from their respective hydrogen evolution rates: 1348 μmol g^{-1} h^{-1} for OVS-Py-BT HPP and a much lower 11.3 μmol g^{-1} h^{-1} for OVS-Py-TPE HPP.

KEYWORDS: *Octavinylsilsesquioxane, Benzothiadiazole, Hybrid porous organic/inorganic polymers, Energy storage, Photocatalytic hydrogen production*

■ INTRODUCTION

A developed porous material, based on polyhedral oligomeric silsesquioxanes (POSS), demonstrates variable properties and a highly symmetrical three-dimensional structure with specified nanometer-sized dimensions.[1−5] Its potential lies in the combination of versatile and flexible organic shells surrounding a rigid silica core. It is a promising candidate for synthesizing hybrid nanocomposites that exhibit properties midway between organics and ceramics,[1−10] The increasing demand for POSS in scientific research and industry is attributed to their customizable physical and chemical properties.[1−8] Another crucial aspect of functionalized silsesquioxanes is their physicochemical properties arising from their hybrid (organic−inorganic) nature.[1−5] The Si−O−Si framework, corresponding to silica with a well-defined structure, could serve as an intriguing material for modifying polymers and acting as fillers (nanofillers).[1−5] The precise control of molecule sizes and the variation in functional groups within the POSS core allow for their accurate deposition and embedding in a polymer matrix.[1−5] This, in turn, results in the creation of composite materials with unique characteristics. These organic−inorganic hybrid materials showcase a diverse range of fascinating physicochemical properties, including alterations in solubility, enhanced dielectric characteristics, improved resistance to oxidation and fire, elevated decomposition and glass transition temperatures, reduced heat transfer rates, and an impact on the hardness of the resulting materials.[1−5]

Received: March 1, 2024
Revised: April 17, 2024
Accepted: April 28, 2024
Published: May 3, 2024

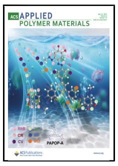

https://doi.org/10.1021/acsapm.4c00655

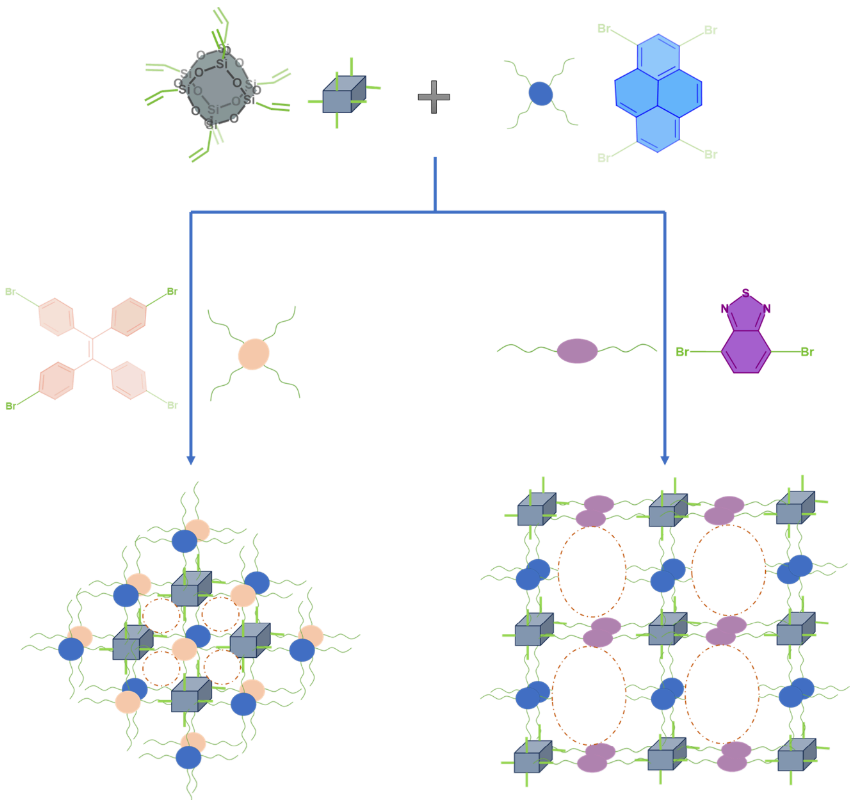

- Highly crosslinking polymer
- Small surface area (77 m^2 g^{-1})
- Low porosity
- HER (40.3 μmol g^{-1} h^{-1})
- Specific apacitance (54 F/g)

- Low crosslinking polymer
- Large surface area (354 m^2 g^{-1})
- High porosity
- HER (1348 μmol g^{-1} h^{-1})
- Specific capacitance (248 F/g)

Figure 1. Schematic diagram shows our design strategy for constructed OVS-based HPPs.

Octavinylsilsesquioxane (OVS), a derivative of cage silsesquioxanes (SQs), proves to be a highly valuable component in the creation of porous materials through diverse methods such as click reactions, Heck reactions, hydrosilylation, and Friedel−Crafts processes. The exceptional optical and electrical properties inherent to OVS are seamlessly transferred to these materials. Additionally, the incorporation of OVS brings the added advantage of modifying the energy gap of the resulting materials. Additionally, the cost-effectiveness of OVS makes it a highly favorable choice for large-scale production.[9−15] Porous organic polymers (POPs) derived from OVS, showcase noteworthy attributes, including impressive surface area, well-defined pore size, heat stability, and excellent electrochemical performance.[16−22]

Supercapacitors (SCs), also referred to as ultracapacitors, are primarily categorized into three types based on the electrode material utilized.[23−26] The ability to store charge depends on the available surface area of the electrode, with a large surface area and very thin dielectric resulting in high capacitance values.[27−29] While the mechanism of charge storage in supercapacitors is similar to conventional capacitors, charges accumulate at the electrode's surface, forming a double layer. In supercapacitors, the movement of ions is governed by electrostatic energy, and nonfaradic reactions predominate, as there is no transfer of electrons between the electrolyte and the electrode.[23,30−34] Capacitance in electrical double-layer capacitors (EDLC) is generated as electrons adhere to ions within the pores of the electrode material.[23] Conversely, in pseudocapacitors, a reversible reaction occurs between the electrode and the electrolyte.[23]

Hydrogen (H_2) fuel is emerging as the most promising environmentally friendly energy source without carbon emissions.[35,36] Water splitting, a key technique for hydrogen fuel production, requires an optimal potential of 1.23 V to efficiently split water into hydrogen and oxygen gas. In practice, this potential often reaches 1.8 V, leading to high thermodynamic process costs.[37,38] The efficiency of water splitting is further challenged by inevitable dynamic overpotential, underscoring the crucial role of photocatalysts in minimizing this overpotential. Noble metal-based photocatalysts, such as Pt/C, are commonly employed for the HER in photochemical water splitting.[39,40] Despite Pt/C exhibiting superior performance in both acidic and alkaline media, its widespread application in HER on a large scale is hindered by its high cost. Consequently, there is a pressing need to explore efficient yet cost-effective non-noble metal-based photocatalysts for HER, particularly in alkaline media.[41,42]

The Py molecule stands out as a renowned chromophore, boasting an exceptional capability as an electron source. Fast electron transport and strong light harvesting are guaranteed by its large π-conjugated structure.[43−46] In comparison to conventional organic molecules, Py-based microporous organic polymers (MOPs) exhibit a remarkable combination of attributes, including a highly accessible surface area, a well-ordered surface structure, and a substantial quantity of active surface sites distributed across expansive areas.[43−46] Con-

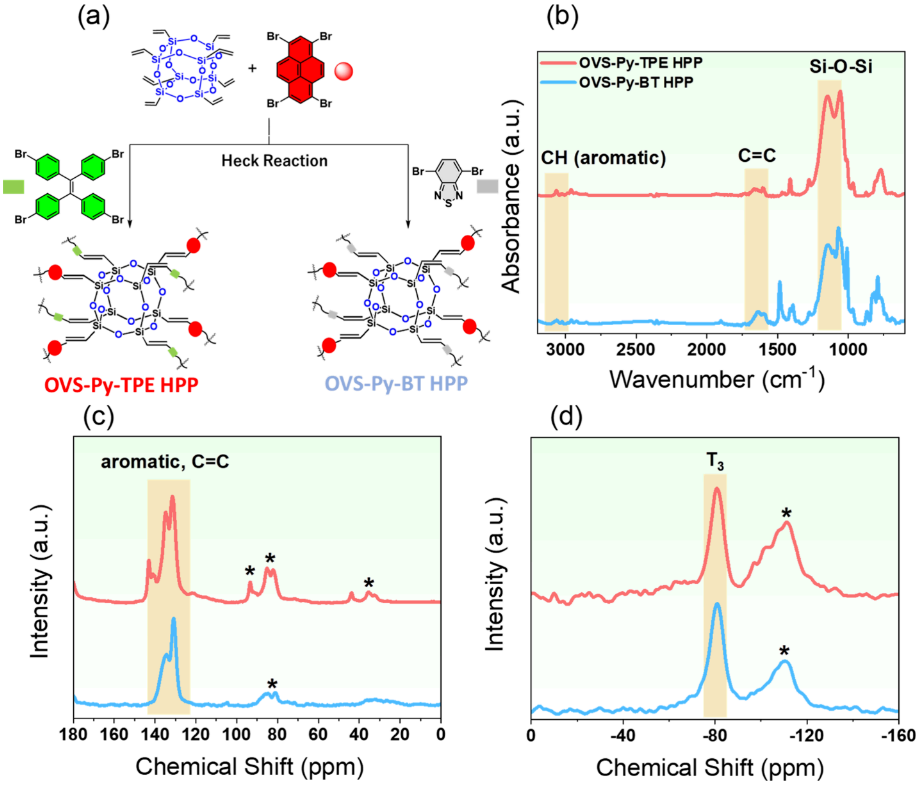

Figure 2. (a) Schematic scheme, (b) FTIR, (c) ^{13}C CP/MAS NMR, and (d) solid-state ^{29}Si MAS NMR of OVS-Py-TPE and OVS-Py-BT HPPs.

sequently, MOPs derived from pyrene have exhibited considerable potential in applications such as photocatalytic H_2 evolution, energy storage, and chemical reaction transformation.[43−46] 2,1,3-benzothiadiazole (BT) could function as a catalytic site for the production of hydrogen in polymer dots photocatalysts.[61−63] Additionally, BT has found extensive use as a unit to block electron acceptance in various organic polymers employed for photocatalysis.[47−50] The utilization of OVS-based porous organic materials in photocatalysis applications is not widespread; however, He group[51] has successfully employed POSS-based POMPs to catalyze the photochemical production of syngas through CO_2 reduction. Mohamed et al. effectively synthesized OVS-P-TPA HPP and OVS−P-F HPP, with promising hydrogen evolution rates (HER) of 701.9 and 56.6 μmol g^{-1} h^{-1}, respectively.[52]

Based on the findings above, we synthesized two varieties of HPPs utilizing (OVS) units through the Heck reaction method. Specifically, OVS was subjected to reactions with Py-Br$_4$/TPE-Br$_4$ (four-branched monomer) and Py-Br$_4$/BT-Br$_2$ (two-branched monomer), resulting in the formation of OVS-Py-TPE and OVS-Py-BT HPPs with a completely different surface area, resulting in high and low cross-linking polymers, then small and large surface area, respectively [Figure 1]. According to Brunauer−Emmett−Teller (BET) calculations, the material synthesized with BT-Br$_4$ exhibits surface areas exceeding 4.5-fold compared to that synthesized with TPE-Br$_4$ quantified at 354 and 77 m^2 g^{-1}, respectively. Remarkably, galvanostatic charge−discharge (GCD) analysis demonstrated excellent performance of OVS-Py-BT HPP in supercapacitor applications, yielding a specific capacitance value of 248 F/g for OVS-Py-BT HPP. The stability of OVS-Py-TPE and OVS-Py-BT HPPs was corroborated by analyzing the percentage capacitance retention, revealing values of 78.0% and 88.7%, respectively, after 2000 cycles. Additionally, the materials underwent characterization for the photocatalytic hydrogen evolution reaction (HER). Results indicated that POSS-Py-BT HPP exhibited superior performance in hydrogen evolution compared to OVS-Py-TPE HPP, with HER values recorded at 40.3 and 1348 μmol g^{-1} h^{-1} for OVS-Py-TPE and OVS-Py-BT HPPs, respectively. Notably, OVS-Py-BT HPP displayed no decrease in HER even during a 20-h, five-cycle long-term assessment.

■ EXPERIMENTAL SECTION

Materials. Sigma−Aldrich supplied benzophenone (BZE, 99%), zinc powder (Zn, 99.99%), titanium chloride ($TiCl_4$, 99.9%), glacial acetic acid (AcOH, 99%), 2,1,3-benzothiadiazole (BT, 98%), pyrene (Py, 98%), Br_2 solution, and potassium carbonate (K_2CO_3, 99%). The Py-Br$_4$, TPE, and TPE-Br$_4$ were synthesized using previously outlined methods, with detailed preparation and spectroscopic analyses available in the Supporting Information.[53−60]

Synthesis of 4,7-Dibromobenzo[c][1,2,5]thiadiazole (BT-Br$_2$). BT (20.0 g, 220.2 mmol) was combined with 160 mL of 48% HBr and 105 g (660.9 mmol) of Br_2 solution. The resulting mixture underwent reflux for 9 h at 95 °C. Upon adding this solution to a NaOH solution at 0 °C, the entire mixture was processed using DCM, forming a white powder (5 g, 50%) identified as BT-Br$_2$. FTIR: 3036 [Figure S1]. ^{1}H NMR: 7.74 ppm [Figure S2]. ^{13}C NMR: 154, 134, 115 ppm [Figure S3].

Synthesis of OVS-Py-TPE and OVS-Py-BT HPP. A mixture composed of 1 mmol of OVS, 0.1 mmol of Py-Br$_4$, 3.8 mmol of TPE-Br$_4$ or BT-Br$_2$, 16 mmol of K_2CO_3, and 0.06 g of $Pd(PPh_3)_4$ in 40 mL of DMF was prepared. The resulting mixture underwent stirring in a nitrogen atmosphere at 110 °C for 3 days. Acetone, THF, water, and MeOH were used as washing agents in a sequence of filtering stages throughout the subsequent purification process, separating the precipitate from the solution cooled to room temperature. The purification process carried out by using Soxhlet extraction [DMF,

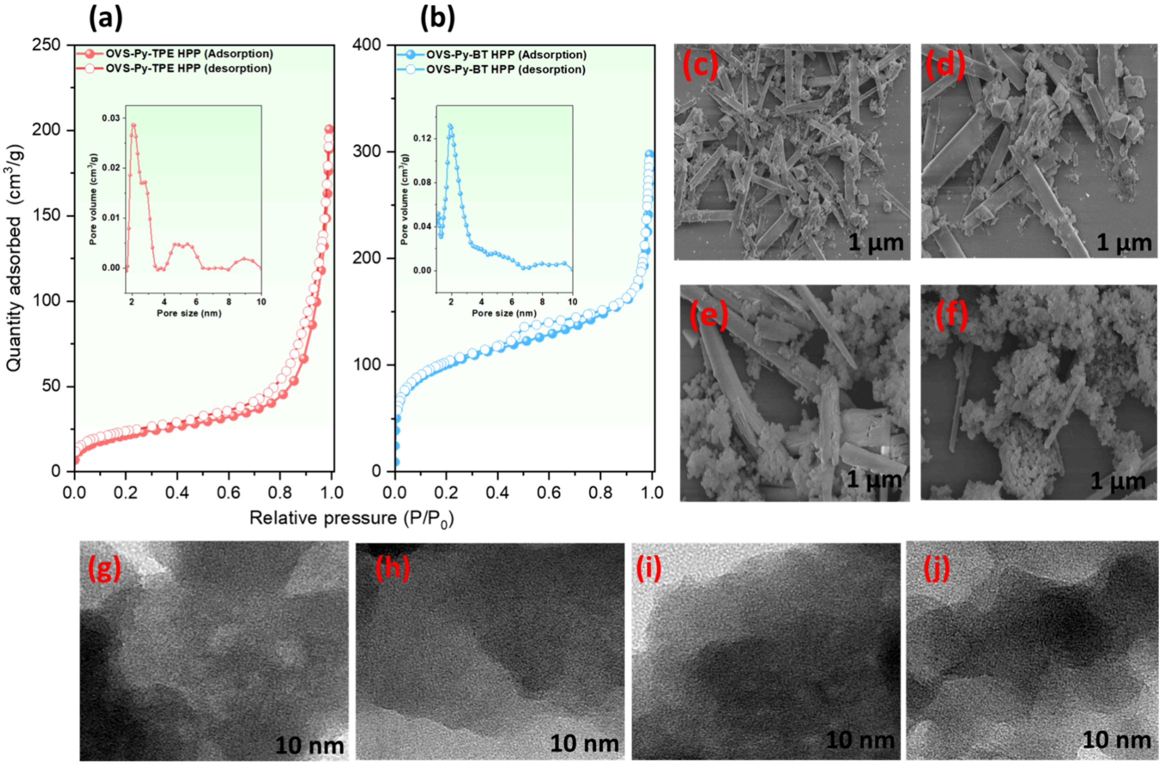

Figure 3. (a, b) BET profiles, (c−f) SEM, and (g−j) TEM images of OVS-Py-TPE (a, c, d, g, h) and OVS-Py-BT HPPs (b, e, f, i, j).

THF, and MeOH] yielded a white powder identified as OVS-Py-TPE HPP and a gray powder identified as OVS-Py-BT HPP.

■ RESULTS AND DISCUSSION

Synthesis and Characterization of OVS-Py-TPE and OVS-Py-BT HPPs. In the synthesis of two types of HPPs, namely OVS-Py-TPE and OVS-Py-BT HPPs (depicted in Figure 2(a)), a Heck coupling reaction was employed. The starting materials for this reaction included Py-Br$_4$/TPE-Br$_4$ and Py-Br$_4$/BT-Br$_2$, with OVS acting as the companion molecule. In Figure 2(a), the occurrence of the Heck reaction is depicted in DMF at 110 °C, facilitated by K_2CO_3 and $Pd(PPh_3)_4$ as catalysts. Figure 2(b) presents the FTIR spectra for both OVS-Py-TPE and OVS-Py-BT HPPs were anticipated to exhibit absorption bands corresponding to C = C stretching vibrations in the range of 1600 to 1590 cm^{-1} and aromatic C−H stretching vibrations between 3080 and 3020 cm^{-1}. Moreover, the formation of cross-linked networks resulting from the successful Heck reaction of OVS with Py-Br$_4$/TPE-Br$_4$ and Py-Br$_4$/BT-Br$_2$ is evident from the broad absorption peak of Si−O−Si (around 1070−1050 cm^{-1}) in these spectra. In Figure 2(c), robust signals were observed in the ^{13}C solid-state NMR spectra of OVS-Py-TPE and OVS-Py-BT HPPs. These signals were associated with carbon resonances within the aromatic units and Si−C = C units present in the OVS cage. The detected signal ranges for OVS-Py-TPE HPP and OVS-Py-BT HPP were 142−119 ppm and 147−125 ppm, respectively. To verify the existence of the OVS cage in OVS-Py-TPE and OVS-Py-BT HPPs, ^{29}Si NMR was employed. In the NMR spectra of these HPPs, T_3 (T_n: $CSi(OSi)_n(OH)_{3-n}$) signals were observed at −83.73 and −83.47 ppm for OVS-Py-TPE and OVS-Py-BT HPPs, respectively (Figure 2(d)). Notably, the preservation of the OVS cage architecture in all synthesized HPPs was evident, indicated by the absence of T_2 signals. Additionally, XPS analysis [Figure S4] confirmed the presence of elements, including C, Si, N, O, and S atoms, in both OVS-Py-TPE and OVS-Py-BT HPPs. For instance, in the OVS-Py-TPE HPP sample, the orbital binding energies of Si 2p, Si 2s, C 1s, and O 1s were determined to be 103.18, 153.37, 284.68, and 532.20 eV, respectively. In the OVS-Py-BT HPP sample, corresponding values were 102.33, 153.36, 173.72, 284.68, 401.03, and 533.17 eV, respectively. The thermal properties of OVS-Py-TPE and OVS-Py-BT HPPs were assessed through TGA, as depicted in Figure S5. Based on the TGA results, OVS-Py-BT HPP exhibited superior thermal stability compared to OVS-Py-TPE HPP, evidenced by a char yield of 73 wt % and thermal degradation temperatures (T_{d10}) reaching 410 °C. The relatively lower thermal stability of OVS-Py-TPE HPP compared to OVS-Py-BT HPP may stem from the susceptibility of the C = C bond within the TPE moiety to degrade more readily at elevated temperatures.

To assess the enduring porosity of the two HPPs, nitrogen sorption isotherms were conducted at 77 K. Figure 3(a) and (b) illustrates the isotherms for OVS-Py-TPE and OVS-Py-BT HPPs, revealing a characteristic combination of type I and IV isotherms indicative of micropores and minute mesopores. According to Brunauer−Emmett−Teller (BET) calculations, the surface areas of OVS-Py-TPE and OVS-Py-BT HPPs were determined to be 77 and 354 m^2 g^{-1}, respectively. In the context of V_{total}, OVS-Py-BT HPP exhibited the highest success, registering a value of 0.44 cm^3 g^{-1}, surpassing OVS-Py-TPE HPP, which recorded a value of 0.29 cm^3 g^{-1}. The pore size distributions of OVS-Py-TPE and OVS-Py-BT HPPs were predominantly concentrated in the 2.04 and 1.90 nm, respectively. These values were determined through calculations employing nonlocal density functional theory (NLDFT). The abundance of micropores and mesopores in

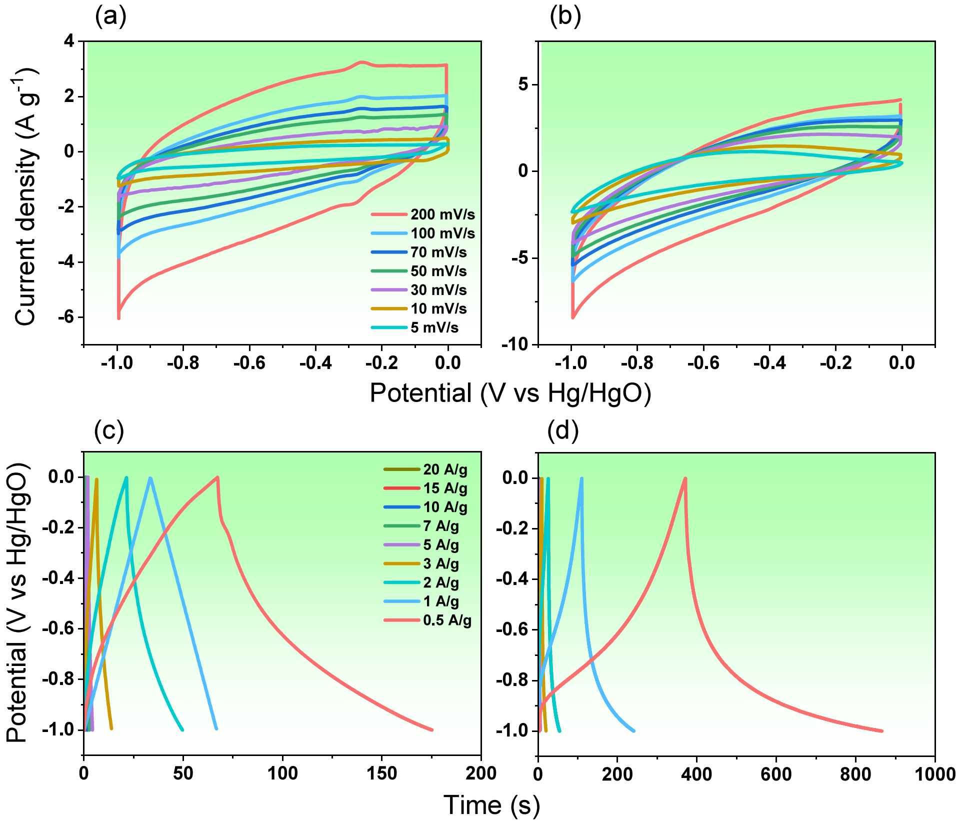

Figure 4. Electrochemical performance of OVS-Py-TPE (a, c) and OVS-Py-BT HPPs (b, d) using CV (a, b) and GCD (c, d) analyses.

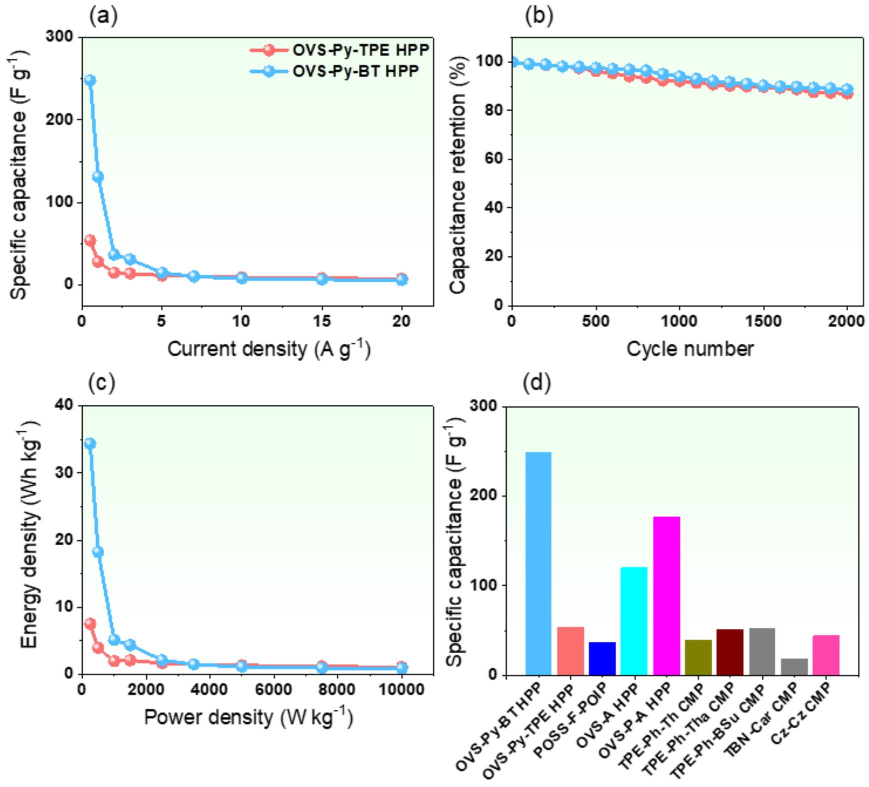

Figure 5. (a) Specific capacitance data derived from GCD profiles, (b) capacitance retention, (c) Ragone plots of OVS-Py-TPE and OVS-Py-BT HPPs, and (d) comparison of specific capacitance data of OVS-Py-TPE and OVS-Py-BT HPPs compared with other organic electrodes.

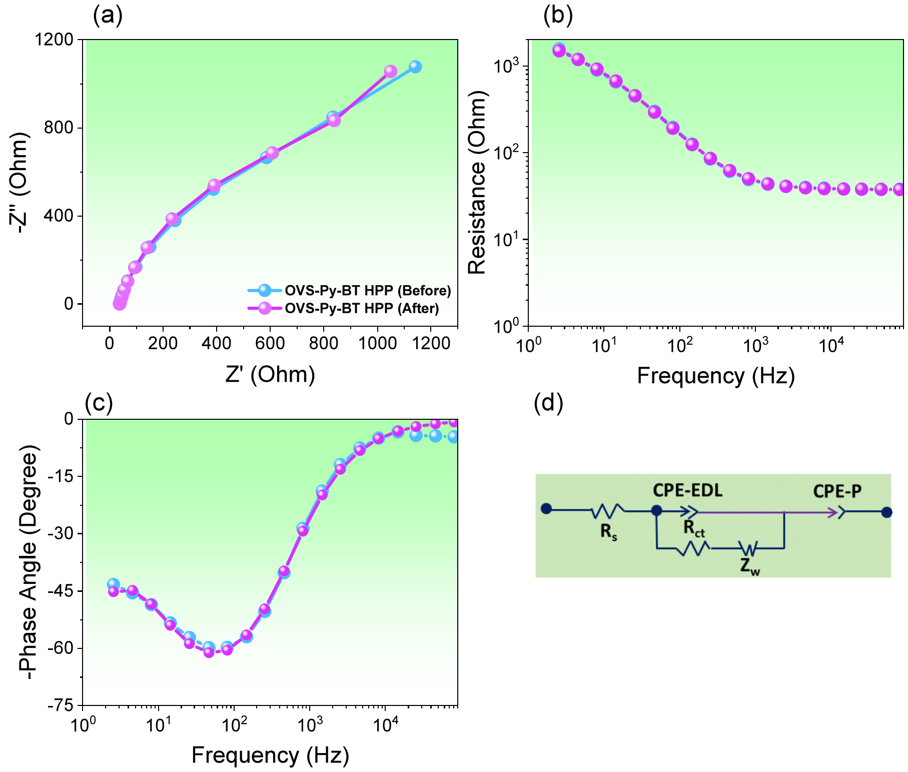

Figure 6. Electrochemical impedance spectrometry curves: (a) Nyquist plots, (b) Bode plot of frequency-dependent resistance (magnitude), (c) Bode plot of frequency-dependent phase angles, and (d) equivalent fitted circuit of OVS-Py-BT HPPs.

OVS-Py-BT HPP suggests the presence of numerous reactive sites conducive to photocatalytic hydrogen (H_2) evolution. Scanning electron microscopy (SEM) images revealed that OVS-Py-TPE HPP exhibits an aggregation structure comprising irregularly elongated columnar and spherical particles, as depicted in Figure 3(c) and (d). In contrast, POSS-Py-BT HPP displays irregularly columnar and cloud-like particles, as shown in Figure 3(e) and (f). TEM images (Figure 3(g–j)) of both OVS-Py-TPE and OVS-Py-BT HPPs revealed a microporous structure lacking long-range order.

Electrochemical Performance of OVS-Py-TPE and OVS-Py-BT HPPs. Electrochemical experiments were conducted using a three-electrode cell setup with a Hg/HgO reference electrode and platinum counter electrode. The working electrode was constructed by applying the slurry onto a glassy carbon electrode. The CV analysis [at different scan rates 5–200 mV s^{-1}] of OVS-Py-TPE and OVS-Py-BT HPPs was carried out in a 1 M KOH electrolyte medium, as illustrated in Figure 4(a) and (b). The CV curves of OVS-Py-TPE and OVS-Py-BT HPPs, characterized by their rectangular-like shapes, showcase the exceptional capacitive behavior of the OVS-Py-TPE and OVS-Py-BT HPPs as electrode materials. This behavior indicates that charges are predominantly stored as electrical double-layer capacitance (EDLC) and pseudocapacitance. Figure 4(c) and (d) illustrates the GCD curves for OVS-Py-TPE and OVS-Py-BT HPPs. These curves were obtained at diverse current densities ranging from 0.5 to 20 A g^{-1}, as depicted in Figure 4, utilizing a three-electrode cell configuration. The symmetric behavior observed in the GCD profiles of both HPPs implies a high level of reversibility in the electrochemical process, even at the notably high current density of 20 A g^{-1}.

Utilizing GCD profiles from Figure 4, the specific capacitance of OVS-Py-TPE and OVS-Py-BT HPPs at various current densities was calculated, as shown in Figure 5(a). For the OVS-Py-TPE HPP sample, specific capacitances were determined to be 248, 131.2, 36.8, 31.2, 15, 10.5, 8.1, 6.6, and 6.1 F g^{-1} at current densities of 20, 15, 10, 7, 5, 3, 2, 1, and 0.5 A g^{-1}, respectively. Similarly, for the OVS-Py-BT HPP sample, specific capacitances were found to be 54, 28.2, 15, 14, 11.8, 9.5, 8.33, and 7.7 F g^{-1} at the corresponding current densities. Elevated ion concentration at the electrode surface can lead to a reduction in specific capacitance for both HPPs, particularly at high current densities, resulting in concentration polarization. This phenomenon has the potential to impede ion transport, decrease capacitance, and limit efficient electrode–electrolyte interactions during rapid charge and discharge cycles.

The data presented in Figure 5(b) reflects the outcomes of 2000 charge and discharge cycles at a 10 A g^{-1}. Both materials demonstrate impressive retention rates, with OVS-Py-TPE HPP showing a retention rate of 87.0%, while OVS-Py-BT HPP exhibits a slightly higher retention rate of 88.7%. According to the Ragone plot presented in Figure 5(c), the OVS-Py-TPE and OVS-Py-BT HPPs exhibited energy densities of 7.5 and 34.5 Wh kg^{1-}. The framework of OVS-Py-BT HPP, depicted in Figure 5(d) and Table S1, exhibits a slightly higher specific capacitance (248 A g^{-1}) compared to OVS-Py-TPE HPP, POSS-F-POIP, OVS-A HPP, OVS-P-A-HPP, TPE-Ph-Th CMP, TBN-Car CMP, Cz-Cz CMP. The remarkable electrochemical properties observed in the CV and GCD results highlight the exceptional performance of OVS-Py-BT HPP. This superiority can be attributed to its conjugated structure, offering increased surface area and enhanced conductivity. These characteristics position it as a promising

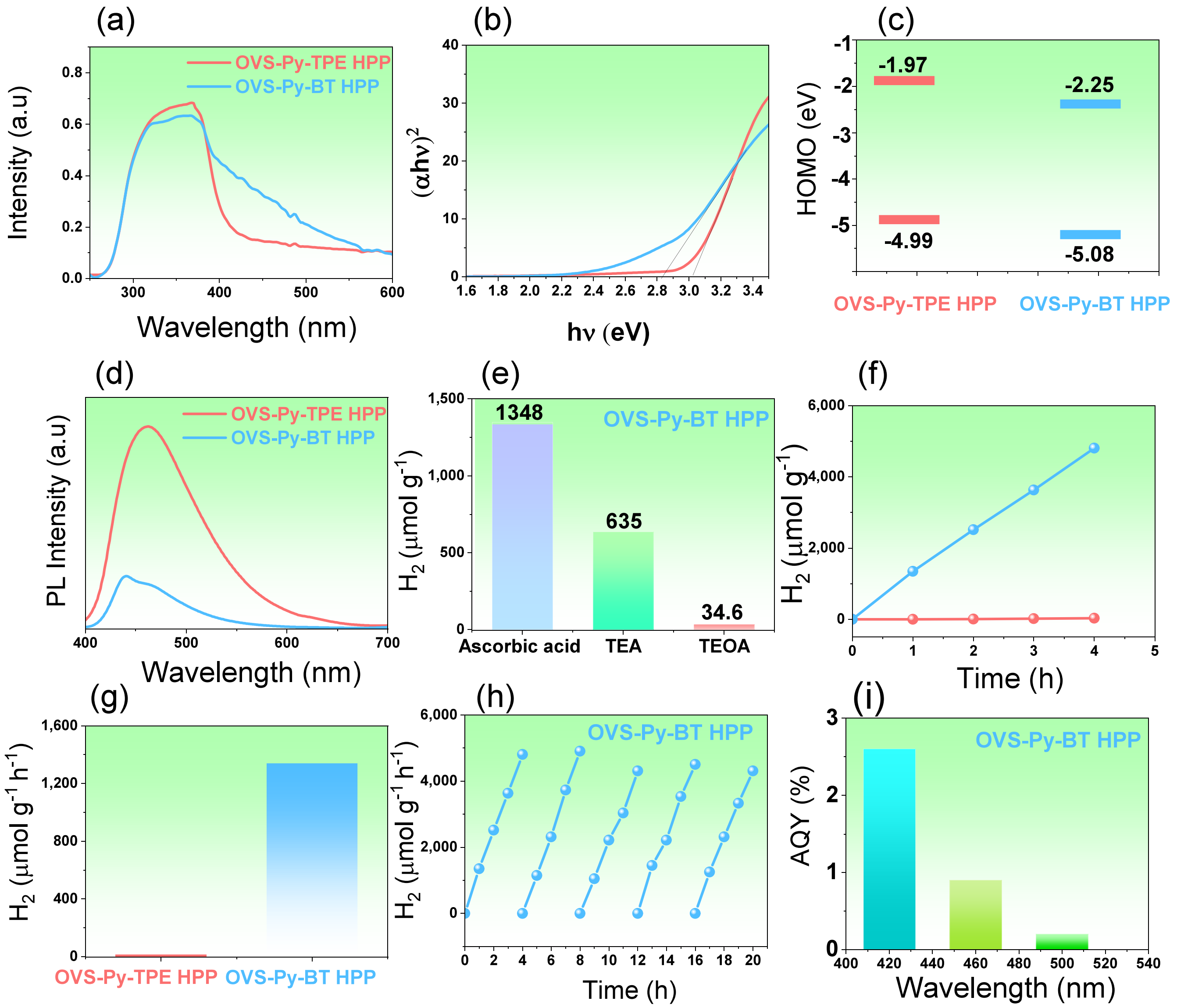

Figure 7. (a) UV−vis absorption spectra, (b) Tauc plots, (c) energy level diagram, (d) PL spectra of OVS-Py-TPE and OVS-Py-BT HPPs photocatalysts, (e) H_2 production of OVS-Py-BT HPP using different sacrificial reagents, (f, g) time-dependent H_2 production and HER for OVS-Py-TPE and OVS-Py-BT HPPs, (h) stability of OVS-Py-BT HPP for H_2 production at different time, and (i) AQYs of the OVS-Py-BT HPP at various wavelengths of light.

material for potential applications in supercapacitors. Applying the principle of ion diffusion, EIS was employed to assess the electrical resistance of multiple electrodes. Represented by the symbols R_1, R_2, CPE-EDL, CPE-P, and Z_w, Figure 6(a−d) displays various Nyquist plots accompanied by corresponding fitted circuits. These plots elucidate distinct characteristics of the electrodes, encompassing charge transfer and series resistances, constant phase elements (CPE-EDL, CPE-P), and Warburg elements (Z_w). The initial ohmic resistance of the OVS-Py-BT HPP electrode measured 37.82 and 37.63 Ohms before and after fitting, underscoring the promising conductivity of OVS-Py-BT HPP as an electrode material. Additionally, the exceptional capacitive performance of the OVS-Py-BT HPP electrode compound for energy applications was illustrated through the frequency-dependent magnitude Bode plot in Figure 6(b). Moreover, the frequency-dependent phase angle Bode plot in Figure 6(c) revealed the knee frequency, a crucial indicator of the rate performance of electrode materials. The knee frequency, measured at a 45° phase angle, is the point at which resistive and capacitive qualities are equal. In Figure 6(c), the indicated knee frequency of 2.55 Hz for OVS-Py-BT HPP underscores its suitability as an electrode for applications in energy storage. Figure 6(d) illustrates the corresponding fitted circuit for OVS-Py-BT HPP.

Photoelectronic Properties and Photocatalytic Hydrogen Production from Water by OVS-Py-TPE and OVS-Py-BT HPPs. The photoelectronic properties of OVS-based HHPs were investigated using UV−vis DRS, Tauc plot analysis, photoluminescence (PL), and photoelectron spectroscopy. Figure 7(a) shows the UV−vis spectra of OVS-Py-TPE and OVS-Py-BT HPPs, revealing absorption peaks at 410.9 and 438.9 nm, respectively. OVS-Py-BT HPPs exhibited a red-shifted absorption onset due to the presence of electron-deficient benzo[d]thiadiazole moieties. This indicates strong light absorption, making them suitable for solar-driven

https://doi.org/10.1021/acsapm.4c00655
ACS Appl. Polym. Mater. 2024, 6, 5945−5956

photochemical reactions. The Tauc plot in Figure 7(b) reveals favorable band gaps of 2.83 eV (OVS-Py-BT HPP) and 3.02 eV (OVS-Py-TPE HPP) for photocatalytic hydrogen production. HOMO levels were determined by UPS, and LUMO levels were calculated were calculated (E_{HOMO} + E_g). The results are summarized in Figure 7(c). HOMO levels are −4.99 eV (OVS-Py-TPE) and −5.08 eV (OVS-Py-BT HPP), and LUMO levels are −1.97 eV and −2.25 eV, respectively. All polymers have LUMO levels above the hydrogen reduction potential, confirming their ability to produce H_2 from water. Photoluminescence (PL) was used to assess the separation efficiency of photogenerated electron−hole pairs in OVS-based HHPs, which impacts photocatalytic efficiency.[61] Lower PL intensity indicates better charge separation. As shown in Figure 7(d), the PL spectra of these materials exhibit different emission bands and intensities under 400 nm excitation. Notably, OVS-Py-BT HPPs display the lowest emission intensity, signifying more efficient generation and separation of photoinduced charge carriers and suppressed exciton recombination, which is beneficial for photocatalytic activity. Based on the ICP-OES data, Pd concentrations in both the OVS-Py-TPE HPP and OVS-Py-BT HPP were measured at 3.5 and 5.5 ppm, respectively [Table S2]. Remarkably, there is minimal deviation in Pd concentration across the displayed OVS-Py-TPE HPP and OVS-Py-BT HPP, suggesting a consistent impact across materials. In terms of photocatalytic activity for H_2 evolution, it is reasonable to deduce that all materials demonstrate this uniform effect.[62] Solar-driven hydrogen evolution was investigated using OVS-Py-TPE HHP and OVS-Py-BT HPP photocatalysts under visible light irradiation (380−780 nm). Hydrogen production was quantified by gas chromatography (GC) over 1 h in a 500 μL photoreactor. Methanol was added to improve catalyst dispersion in water, and ascorbic acid (AA) was used as a sacrificial electron donor (SED) to promote the reaction. Ascorbic acid was the most effective sacrificial donor compared to TEOA and TEA, leading to a significantly higher hydrogen evolution rate (HER) of 1348 μmol g^{-1} h^{-1} for OVS-Py-BT HPP (Figure 7(e)). Figure 7(f) compares the H_2 evolution over time for OVS-Py-BT HPP and OVS-Py-TPE HPP. OVS-Py-BT HPP exhibits a significantly steeper curve, indicating a much faster HER. The lower HER of OVS-Py-TPE HPP (11.4 μmol g^{-1} h^{-1}) is reflected in its nearly flat curve (Figure 7(g)). This excellent performance of OVS-Py-BT HPP is attributed to its enhanced photocurrent response and efficient charge carrier separation, which minimizes recombination. The stability and reusability of OVS-Py-BT HPP were evaluated over five cycles (20 h total). The photocatalytic activity and hydrogen production rate remained consistent, demonstrating the catalyst's stability against photocorrosion under visible light (Figure 7(h)). This confirms the excellent performance of OVS-Py-BT HPP for hydrogen evolution. The apparent quantum yield (AQY) of OVS-Py-BT HPP for hydrogen production was measured under monochromatic light. AQY values were 2.6%, 0.9%, and 0.2% at 420, 440, and 500 nm, respectively (Figure 7(i)). Additionally, static water contact angles were determined using the sessile drop technique. OVS-Py-BT HPP exhibited lower water contact angles compared to OVS-Py-TPE HPP (see Figure S6), indicating greater hydrophilicity. This suggests that replacing the tetra-branched TPE moiety with the dibranched BT moiety improves water dispersibility, likely due to the increased surface area and porosity of OVS-Py-BT HPP. Overall, the substitution of TPE with BT offers a promising strategy for enhancing water dispersibility and promoting hydrogen production from water.

The density-functional theory (DFT) of the DMol3 code[63] was used to obtain the optimized structure and electronic properties. The electrical and optical characteristics of OVS-Py-TPE and OVS-Py-BT HPPs were determined in this work using ab initio calculations based on DFT. The FMO's work[64] sheds light on possible theories for intramolecular electron transport and delocalization. The influence of donor and acceptor fragments on the photoelectric properties of OVS-Py-TPE and OVS-Py-BT HPPs was examined by our investigation, which included the determination of the bandgap, HOMO and LUMO energy levels, and chemical reactivity indices (Table S3). We provide the HOMO−LUMO energies with bandgap energy (E_g) of the OVS-Py-TPE and OVS-Py-BT HPPs substituted systems [Figure 7(i)]. The bandgap energy is the most critical factor in the photocatalytic process since it offers valuable information for charge transfer and photocatalytic activity. According to the lower energy gap value (E_g), the best photocatalyst is OVS-Py-BT HPP, which agrees with the H_2 evolution results. It found that, with increasing π conjugation length, the HOMO−LUMO gap decreases, and the use of heteroatoms (N and S) in OVS-Py-BT HPP framework[65,66] which facilitates electron transfer from HOMOs to LUMOs, thus enhancing the photocatalytic activity. Therefore, the OVS-Py-BT HPP with the lowest bandgap energy is considered the best photocatalyst for H_2 evolution, which agrees with the experimental findings. In the OVS-Py-BT HPP, the LUMO orbital predominantly resides over the benzothiadiazole ring, while the HOMO orbital is primarily concentrated over the pyrene donor, as depicted in Figure 8. This orbital distribution implies that, when it comes to separating photogenerated electron−hole (e^-/h^+) pairs, the OVS-Py-BT HPP is expected to outperform other molecules in terms of photocatalytic efficiency. The observed pattern during light irradiation suggests robust electron delocalization and

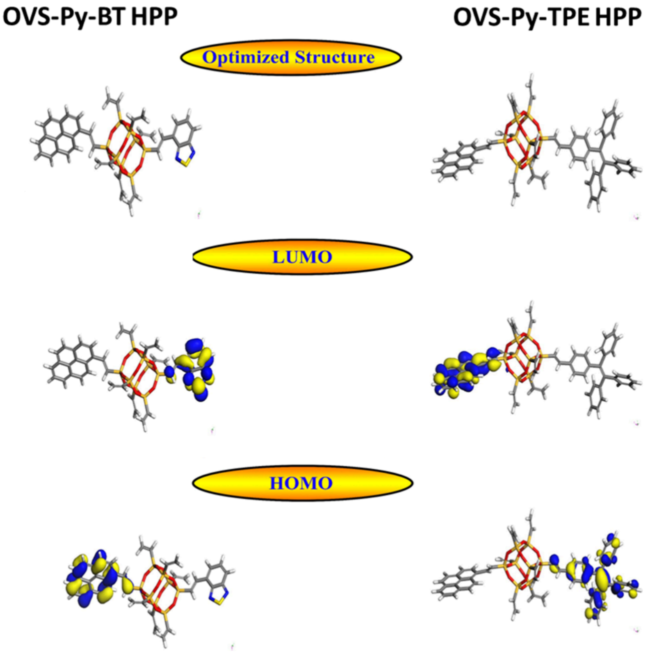

Figure 8. Optimized geometries and density of HOMO and LUMO frontier molecular orbitals of OVS-Py-TPE and OVS-Py-BT HPPs.

significant charge transfer (CT) within the examined molecule. On the other hand, the OVS-Py-BT HPP has the lowest conduction (CB) and energy gap (E_g) than other compounds [Figure 7(i)], suggesting that it has superior charge transfer, red-shifted absorption, and enhances photocatalytic performance. The density of states is a valuable method for analyzing the influence of electron distribution on the catalyst surface. Additionally, we performed the partial density of states (PDOS) analysis for the OVS-Py-BT HPP molecule (see Figure S7). The analysis results demonstrate that a new state appears between CB and VB due to the S2*p* and N2*p* orbitals contribution of the BT ring, which reduces the E_g and can potentially improve the efficiency of visible light absorbance. The calculated PDOS of orbital contribution for each atom indicates that the conduction band (CB) mainly consists of 2p orbitals of C, N, and S atoms with a small contribution of Si and O atoms. Meanwhile, the valence band (VB) is mainly composed of the 2s and 2p hybridized orbitals of both C and O atoms with a small contribution of Si, N, and S atoms. The factors of chemical reactivity can be conducted to evaluate the photoelectric properties of molecules. Based on the HOMO and LUMO energy levels of the examined compounds, chemical reactivity parameters such as electron affinity (A), ionization potential (I), electronegativity (χ), electrophilicity index (ω), absolute softness (S), and hardness (η) were computed (Table S3). Chemical hardness describes the resistance of molecules to intramolecular charge transfer,[66,67] therefore, the lower the chemical hardness, the greater the intramolecular charge transfer. Table S3 shows that OVS-Py-BT HPP has the lowest chemical hardness (0.8 eV), which has donor atoms (N and S) with a high π bonds conjugation and the lowest E_g, followed by OVS-Py-TPE HPP (1.14 eV). The electrophilicity index represents the molecule's stability in the presence of external charges to the system.[66,68] In Table S3, the molecule with higher stability is OVS-Py-BT HPP (11.45 eV). On the other hand, the higher electronegativity value (4.28) indicates that the OVS-Py-BT HPP is more capable of accepting electrons, and therefore the chemical activity will be improved. The OVS-Py-BT HPP enhances the photocatalytic performance of HER, showcasing superior photoelectric characteristics according to chemical reactivity criteria. The cost-effective TD-DFT approach can give useful insight into the estimated optical properties of the studied molecules, as well as study the effect of varying other units on the absorption spectra.[69] In the gas phase, the optical absorption spectra were simulated using the TD-DFT/GGA/PBE method. As shown in Figure S8, all the investigated compounds have maximum absorption bands in the visible region. Moreover, the OVS-Py-BT HPP has a more significant overlap area with visible light (~350−800 nm). Compared to other compounds, we observed that introducing a BT unit in the OVS-Py-BT HPP promotes UV−vis absorption compared to other systems, indicating that the BT improves electron delocalization and optical properties. As demonstrated in Figure S8, the OVS-Py-BT HPP has a maximum wavelength of 417 nm (HOMO → LUMO transition) with a small absorbance appearing at 775 nm (HOMO → LUMO+1 transition). The excitation energy of 775 nm, which does not exist in the other molecules, is characterized as the band gap (HOMO−LUMO gap) absorption. Therefore, incorporating donor atoms (N and S) and expanding the π-conjugated network in the OVS-Py-BT HPP molecule can reduce the HOMO−LUMO gap and enhance the light response range. The reaction process was simulated using DFT calculations to get a deeper insight into the active sites of OVS-Py-BT HPP for the H_2 evolution reaction. Accordingly, the Gibbs free-energy changes (ΔG) of hydrogen adsorption involved in the water-splitting process on various atoms (sites 1 to 9) of OVS-Py-BT HPP were calculated (Figure 9). Generally, a lower ΔG_{H*} value indicates better HER activity.[70] Fascinatingly, the adsorbed H* intermediate generated on the pyrene-substituted vinyl group (site 7) of OVS-Py-BT HPP exhibits the lowest energy barrier (0.97 eV) relative to other sites and is regarded as the dominant active site for photocatalytic H_2 evolution (Figure 9).

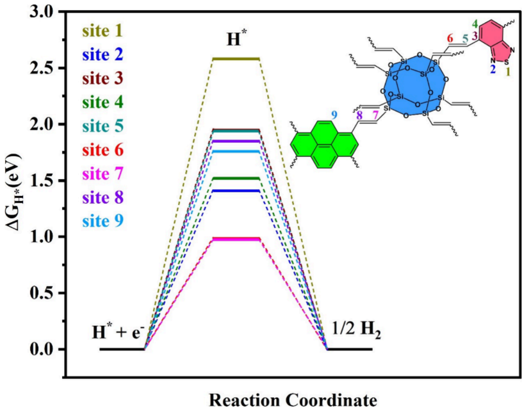

Figure 9. Calculated free-energies diagram (eV) at different active sites of HER on OVS-Py-BT HPP via a single-site reaction pathway.

CONCLUSIONS

In summary, the effective utilization of the Heck coupling reaction has led to the successful development of OVS-Py-TPE and OVS-Py-BT HPPs, showcasing their potential applications in supercapacitors and the synthesis of H_2 from water. When assessing supercapacitor performance, OVS-Py-BT HPP surpasses OVS-Py-TPE HPP in terms of capacitance. Demonstrating considerable promise for supercapacitor applications, OVS-Py-BT HPP exhibits a specific capacitance of 248 F/g and an impressive capacitance retention of 88.5% after 2000 cycles. OVS-Py-BT HPP demonstrates considerable photocatalytic performance for hydrogen evolution (HER), achieving a rate of 1348 μmol g^{-1} h^{-1} with AA as a SED. Notably, the material exhibits excellent stability and reusability, maintaining its activity for over 20 h of continuous use. This excellent stability and performance stem from efficient charge separation, a reduced bandgap, and a lower energy barrier for H_2 generation, as corroborated by experimental and theoretical data. These promising characteristics position OVS-Py-BT HPP as a potential candidate for materials development in both hydrogen evolution and supercapacitors, paving the way for advancements in these critical fields.

ASSOCIATED CONTENT

Supporting Information

The Supporting Information is available free of charge at https://pubs.acs.org/doi/10.1021/acsapm.4c00655.

Details about characterization methods and electrochemical analysis, synthesis of monomers, FTIR, NMR, and comparison of specific capacitance of OVS-Py-TPE

HPP and OVS-Py-BT HPP with those of previously reported materials for supercapacitor application (PDF)

AUTHOR INFORMATION

Corresponding Authors

Mohamed Gamal Mohamed − *Department of Materials and Optoelectronic Science, College of Semiconductor and Advanced Technology Research, Center for Functional Polymers and Supramolecular Materials, National Sun Yat-sen University, Kaohsiung 804, Taiwan; Chemistry Department, Faculty of Science, Assiut University, Assiut 71515, Egypt;* orcid.org/0000-0003-0301-8372; Email: mgamal.eldin12@yahoo.com

Mohamed Hammad Elsayed − *Department of Chemistry, Faculty of Science, Al-Azhar University, Nasr City, Cairo 11884, Egypt; Institute of Atomic and Molecular Sciences, Academia Sinica, Taipei 10617, Taiwan; Center for Condensed Matter Sciences, National Taiwan University, Taipei 10617, Taiwan;* Email: Mohamed.hammad@azhar.edu.eg

Shiao-Wei Kuo − *Department of Materials and Optoelectronic Science, College of Semiconductor and Advanced Technology Research, Center for Functional Polymers and Supramolecular Materials, National Sun Yat-sen University, Kaohsiung 804, Taiwan; Department of Medicinal and Applied Chemistry, Kaohsiung Medical University, Kaohsiung 807, Taiwan;* orcid.org/0000-0002-4306-7171; Email: kuosw@faculty.nsysu.edu.tw

Authors

Ahmed E. Hassan − *Department of Chemistry, Faculty of Science, Al-Azhar University, Nasr City, Cairo 11884, Egypt*

Abdul Basit − *Department of Materials and Optoelectronic Science, College of Semiconductor and Advanced Technology Research, Center for Functional Polymers and Supramolecular Materials, National Sun Yat-sen University, Kaohsiung 804, Taiwan*

Islam M. A. Mekhemer − *Department of Chemical Engineering, National Tsing Hua University, Hsinchu 300044, Taiwan;* orcid.org/0000-0002-0174-6694

Ho-Hsiu Chou − *Department of Chemical Engineering, National Tsing Hua University, Hsinchu 300044, Taiwan;* orcid.org/0000-0003-3777-2277

Kuei-Hsien Chen − *Institute of Atomic and Molecular Sciences, Academia Sinica, Taipei 10617, Taiwan; Center for Condensed Matter Sciences, National Taiwan University, Taipei 10617, Taiwan;* orcid.org/0000-0002-9397-2516

Complete contact information is available at: https://pubs.acs.org/10.1021/acsapm.4c00655

Notes

The authors declare no competing financial interest.

ACKNOWLEDGMENTS

This study was supported financially by the Ministry of Science and Technology, Taiwan, under contracts NSTC 110-2124-M-002-013 and 111-2223-E-110-004. The authors thank the staff at National Sun Yat-sen University for their assistance with the TEM (ID: EM022600) experiments.

REFERENCES

(1) Du, Y.; Liu, H. Cage-like Silsesquioxanes-Based Hybrid Materials. *Dalton Trans.* **2020**, *49*, 5396−5405.

(2) Chen, C. Y.; Chen, W. C.; Mohamed, M. G.; Chen, Z. Y.; Kuo, S. W. Highly Thermally Stable, Reversible and Flexible Main Chain-Type Benzoxazine Hybrid Incorporating Both Polydimethylsiloxane and Double-Decker-Shaped Polyhedral Silsesquioxane. *Macromol. Rapid Commun.* **2023**, *44*, 2200910.

(3) Mohamed, M. G.; Kuo, S. W. Progress in the self-assembly of organic/inorganic polyhedral oligomeric silsesquioxane (POSS) hybrids. *Soft Matter* **2022**, *18*, 5535−5561.

(4) Chiang, C. H.; Mohamed, M. G.; Chen, W. C.; Madhu, M.; Tseng, W. L.; Kuo, S. W. Construction of Fluorescent Conjugated Polytriazole Containing Double-Decker Silsesquioxane: Click Polymerization and Thermal Stability. *Polymers* **2023**, *15*, 331.

(5) Wang, Q.; Unno, M.; Liu, H. Ultrafast and highly selective gold recovery with high capture capacity from electronic waste by upconversion of a silsesquioxane-based hybrid luminescent aerogel. *J. Mater. Chem. A* **2024**, *12*, 5679−5691.

(6) Li, W.; Liu, H. Novel organic-inorganic hybrid polymer based on fluorinated polyhedral oligomeric silsesquioxanes for stable superamphiphobic fabrics and aluminum corrosion protection. *Mater. Today Chem.* **2023**, *29*, 101390.

(7) Mohamed, M. G.; Kuo, S. W. Functional Silica and Carbon Nanocomposites Based on Polybenzoxazines. *Macromol. Chem. Phys.* **2019**, *220*, 1800306.

(8) Wang, Q.; Unno, M.; Liu, H. Dual-Function Near-Infrared Emitting Aerogel-Based Device for Detection and Sunlight-Driven Photodegradation of Antibiotics: Realizing the Processability of Silsesquioxane-Based Fluorescent Porous Materials. *Adv. Funct. Mater.* **2023**, *33*, 2214875.

(9) Yan, Y.; Yang, H.; Liu, H. Silsesquioxane-based fluorescent nanoporous polymer derived from a novel AIE chromophore for concurrent detection and adsorption of Ru^{3+}. *Sens. Actuators B* **2020**, *319*, 128154.

(10) Chou, T. C.; Chen, W. C.; Mohamed, M. G.; Huang, Y. C.; Kuo, S. W. Organic-Inorganic Phenolic/POSS Hybrids Provide Highly Ordered Mesoporous Structures Templated by High Thermal Stability of PS-b-P4VP Diblock Copolymer. *Chem.—Eur. J.* **2023**, *29*, No. e202300538.

(11) Huang, H.; Meng, C.; Xu, Z.; Wang, S.; Chang, Y.; Wang, S.; Chen, J.; Long, Z.; Chen, G. Construction of silsesquioxane and phosphinum-based ionic porous hypercrosslinked polymers for efficient heterogeneous catalytic CO_2 cycloaddition. *J. Polym. Sci.* **2024**, *62*, 1686.

(12) Chen, G.; Huang, X.; Zhang, Y.; Sun, M.; Shen, J.; Huang, R.; Tong, M.; Long, Z.; Wang, X. Constructing POSS and viologen-linked porous cationic frameworks induced by the Zincke reaction for efficient CO_2 capture and conversion. *Chem. Commun.* **2018**, *54*, 12174−12177.

(13) Chen, Z.; Wang, D.; Feng, S.; Liu, H. An Imidazole Thione-Modified Polyhedral Oligomeric Silsesquioxane for Selective Detection and Adsorptive Recovery of Au (III) from Aqueous Solutions. *ACS Appl. Mater. Interfaces* **2021**, *13*, 23592−23605.

(14) Ejaz, M.; Samy, M. M.; Ye, Y.; Kuo, S. W.; Mohamed, M. G. Design Hybrid Porous Organic/Inorganic Polymers Containing Polyhedral Oligomeric Silsesquioxane/Pyrene/Anthracene Moieties as a High-Performance Electrode for Supercapacitor. *Int. J. Mol. Sci.* **2023**, *24*, 2501.

(15) Wang, Q.; Unno, M.; Liu, H. Organic-Inorganic Hybrid Near-Infrared Emitting Porous Polymer for Detection and Photodegradation of Antibiotics. *ACS Sustainable Chem. Eng.* **2022**, *10*, 7309−7320.

(16) Wang, Z.; Kunthom, R.; Kostjuk, S. V.; Liu, H. Near-infrared-emitting silsesquioxane-based porous polymer containing thiophene for highly efficient adsorption and detection of iodine vapor and solution phase. *Eur. Polym. J.* **2023**, *192*, 112072.

(17) Wang, Z.; Mathew, A.; Liu, H. Silsesquioxane-based porous polymer derived from organic chromophore with AIE characteristics

for selective detection of 2,4-dinitrophenol and Ru^{3+}. *Polymer* **2022**, *248*, 124788.

(18) Mohamed, M. G.; Tsai, M. Y.; Wang, C. F.; Huang, C. F.; Danko, M.; Dai, L.; Chen, T.; Kuo, S. W. Multifunctional polyhedral oligomeric silsesquioxane (POSS) based hybrid porous materials for CO_2 uptake and iodine adsorption. *Polymers* **2021**, *13*, 221.

(19) Mohamed, M. G.; Mansoure, T. H.; Takashi, Y.; Samy, M. M.; Chen, T.; Kuo, S. W. Ultrastable porous organic/inorganic polymers based on polyhedral oligomeric silsesquioxane (POSS) hybrids exhibiting high performance for thermal property and energy storage. *Microporous Mesoporous Mater.* **2021**, *328*, 111505.

(20) Liu, Y.; Li, Y.; Koo, S.; Sun, Y.; Liu, Y.; Liu, X.; Pan, Y.; Zhang, Z.; Du, M.; Lu, S.; Qiao, X.; Gao, J.; Wang, X.; Deng, Z.; Meng, X.; Xiao, Y.; Kim, J. S.; Hong, X. Versatile Types of Inorganic/Organic NIR-IIa/IIb Fluorophores: From Strategic Design toward Molecular Imaging and Theranostics. *Chem. Rev.* **2022**, *122*, 209−268.

(21) Ejaz, M.; Mohamed, M. G.; Sharma, S. U.; Lee, J. T.; Huang, C. F.; Chen, T.; Kuo, S. W. An Ultrastable Porous Polyhedral Oligomeric Silsesquioxane/Tetraphenylthiophene Hybrid as a High-Performance Electrode for Supercapacitors. *Molecules* **2022**, *27*, 6238.

(22) Hsiao, C. W.; Elewa, A. M.; Mohamed, M. G.; Kuo, S. W. Highly stable hybrid porous polymers containing polyhedral oligomeric silsesquioxane (POSS)/Dibenzo[g,p]chrysene and Dibenzo[b,d]thiophene units for efficient Rhodamine B dye removal. *Sep. Purif. Technol.* **2024**, *332*, 125771.

(23) Mousa, A. O.; Mohamed, M. G.; Chuang, C. H.; Kuo, S. W. Carbonized Aminal-Linked Porous Organic Polymers Containing Pyrene and Triazine Units for Gas Uptake and Energy Storage. *Polymers* **2023**, *15*, 1891.

(24) Mohamed, M. G.; Chang, W. C.; Chaganti, S. V.; Sharma, S. U.; Lee, J. T.; Kuo, S. W. Dispersion of ultrastable crown-ether-functionalized triphenylamine and pyrene-linked porous organic conjugated polymers with single-walled carbon nanotubes as high-performance electrodes for supercapacitors. *Polym. Chem.* **2023**, *14*, 4589−4601.

(25) Samy, M. M.; Mohamed, M. G.; Kuo, S. W. Conjugated Microporous Polymers Based on Ferrocene Units as Highly Efficient Electrodes for Energy Storage. *Polymers* **2023**, *15*, 1095.

(26) Mousa, A. O.; Chuang, C. H.; Kuo, S. W.; Mohamed, M. G. Strategic Design and Synthesis of Ferrocene Linked Porous Organic Frameworks toward Tunable CO_2 Capture and Energy Storage. *Int. J. Mol. Sci.* **2023**, *24*, 12371.

(27) Mohamed, M. G.; Chang, S. Y.; Ejaz, M.; Samy, M. M.; Mousa, A. O.; Kuo, S. W. Design and Synthesis of Bisulfone-Linked Two-Dimensional Conjugated Microporous Polymers for CO_2 adsorption and Energy Storage. *Molecules* **2023**, *28*, 3234.

(28) Ejaz, M.; Mohamed, M. G.; Huang, W. C.; Kuo, S. W. Pyrene-based covalent organic polymers with nano carbonaceous composites for efficient supercapacitive energy storage. *J. Mater. Chem. A* **2023**, *11*, 22868−22883.

(29) Chen, C. Y.; Mohamed, M. G.; Chen, W. C.; Kuo, S. W. Construction of Ultrastable porous carbons materials derived from organic/inorganic double-decker silsesquioxane (DDSQ) hybrid as a high-performance electrode for supercapacitor. *Mater. Today Chem.* **2023**, *34*, 101773.

(30) Singh, P. N.; Mohamed, M. G.; Chaganti, S. V.; Sharma, S. U.; Ejaz, M.; Lee, J. T.; Kuo, S. W. Rational Design of Ultrastable Conjugated Microporous Polymers Based on Pyrene and Perylene Units as High-Performance Organic Electrode Materials for Supercapacitor Applications. *ACS Appl. Energy Mater.* **2023**, *6*, 8277−8287.

(31) Mohamed, M. G.; Mansoure, T. H.; Samy, M. M.; Takashi, Y.; Mohammed, A. A. K.; Ahamad, T.; Alshehri, S. M.; Kim, J.; Matsagar, B. M.; Wu, K. C.-W.; Kuo, S.-W. Ultrastable Conjugated Microporous Polymers Containing Benzobisthiadiazole and Pyrene Building Blocks for Energy Storage Applications. *Molecules* **2022**, *27*, 2025.

(32) Mohamed, M. G.; Chen, T.-C.; Kuo, S.-W. Solid-state chemical transformations to enhance gas capture in benzoxazine-linked conjugated microporous polymers. *Macromolecules* **2021**, *54*, 5866−5877.

(33) Weng, T. H.; Mohamed, M. G.; Sharma, S. U.; Chaganti, S. V.; Samy, M. M.; Lee, J. T.; Kuo, S. W. Ultrastable three-dimensional triptycene-and tetraphenylethene-conjugated microporous polymers for energy storage. *ACS Appl. Energy Mater.* **2022**, *5*, 14239−14249.

(34) Mohamed, M. G.; Hu, H. Y.; Madhu, M.; Samy, M. M.; Mekhemer, I. M. A.; Tseng, W. L.; Chou, H. H.; Kuo, S. W. Ultrastable Two-Dimensional Fluorescent Conjugated Microporous Polymers Containing Pyrene and Fluorene Units for Metal Ion Sensing and Energy Storage. *Eur. Polym. J.* **2023**, *189*, 111980.

(35) Wang, S.; Lu, A.; Zhong, C. J. Hydrogen production from water electrolysis: role of catalysts. *Nano Convergence* **2021**, *8*, 4.

(36) Mohamed, M. G.; Elsayed, M. H.; Li, C. J.; Hassan, A. E.; Mekhemer, I. M. A.; Musa, A. F.; Hussien, M. K.; Chen, L. C.; Chen, K. H.; Chou, H. H.; Kuo, S. W. Reticular design and alkyne bridge engineering in donor-π-acceptor type conjugated microporous polymers for boosting photocatalytic hydrogen evolution. *J. Mater. Chem. A* **2024**, *12*, 7693−7710.

(37) Li, X.; Zhao, L.; Yu, J.; Liu, X.; Zhang, X.; Liu, H.; Zhou, W. Water Splitting: From Electrode to Green Energy System. *Nano-Micro Lett.* **2020**, *12*, 131.

(38) Yang, Y.; Zhang, K.; Lin, H.; Li, X.; Chan, H. C.; Yang, L.; Gao, Q. MoS_2-Ni_3S_2 Heteronanorods as Efficient and Stable Bifunctional Electrocatalysts for Overall Water Splitting. *ACS Catal.* **2017**, *7*, 2357−2366.

(39) Suryanto, B. H. R.; Wang, Y.; Hocking, R. K.; Adamson, W.; Zhao, C. Overall electrochemical splitting of water at the heterogeneous interface of nickel and iron oxide. *Nature Commun.* **2019**, *10*, 5599.

(40) Li, C.; Baek, J. B. Recent Advances in Noble Metal (Pt, Ru, and Ir)-Based Electrocatalysts for Efficient Hydrogen Evolution Reaction. *ACS Omega* **2020**, *5*, 31−40.

(41) Wu, T.; Sun, M. Z.; Huang, B. L. Non-noble metal-based bifunctional electrocatalysts for hydrogen production. *Rare Met.* **2022**, *41*, 2169−2183.

(42) Wu, H.; Feng, C.; Zhang, L.; Zhang, J.; Wilkinson, D. P. Non-noble Metal Electrocatalysts for the Hydrogen Evolution Reaction in Water Electrolysis. *Electrochem. Energy Rev.* **2021**, *4*, 473−507.

(43) Sun, J.; Sekhar Jena, H.; Krishnaraj, C.; Singh Rawat, K.; Abednatanzi, S.; Chakraborty, J.; Laemont, A.; Liu, W.; Chen, H.; Liu, Y.-Y.; Leus, K.; Vrielinck, H.; Van Speybroeck, V.; Van Der Voort, P. Pyrene-Based Covalent Organic Frameworks for Photocatalytic Hydrogen Peroxide Production. *Angew. Chem. Int. Ed.* **2023**, *62*, No. e202216719.

(44) Samy, M. M.; Mekhemer, I. M. A.; Mohamed, M. G.; Elsayed, M. H.; Lin, K. H.; Chen, Y. K.; Wu, T. L.; Chou, H. H.; Kuo, S. W. Conjugated microporous polymers incorporating Thiazolo[5,4-d]-thiazole moieties for Sunlight-Driven hydrogen production from water. *Chem. Eng. J.* **2022**, *446*, 137158.

(45) Chung, W. T.; Mekhemer, I. M. A.; Mohamed, M. G.; Elewa, A. M.; EL-Mahdy, A. F. M.; Chou, H. H.; Kuo, S. W.; Wu, K. C. W. Recent advances in metal/covalent organic frameworks based materials: Their synthesis, structure design and potential applications for hydrogen production. *Coord. Chem. Rev.* **2023**, *483*, 215066.

(46) Mohamed, M. G.; Elsayed, M. H.; Elewa, A. M.; EL-Mahdy, A. F. M.; Yang, C. H.; Mohammed, A. A. K.; Chou, H. H.; Kuo, S. W. Pyrene-containing conjugated organic microporous polymers for photocatalytic hydrogen evolution from water. *Catal. Sci. Technol.* **2021**, *11*, 2229−2241.

(47) Axelsson, M.; Marchiori, C. F. N.; Huang, P.; Araujo, C. M.; Tian, H. Small Organic Molecule Based on Benzothiadiazole for Electrocatalytic Hydrogen Production. *J. Am. Chem. Soc.* **2021**, *143*, 21229−21233.

(48) Yang, C.; Ma, B. C.; Zhang, L.; Lin, S.; Ghasimi, S.; Landfester, K.; Zhang, K. A. I.; Wang, X. Molecular Engineering of Conjugated Polybenzothiadiazoles for Enhanced Hydrogen Production by Photosynthesis. *Angew. Angew. Chem., Int. Ed.* **2016**, *128*, 9348−9352.

(49) Wang, L.; Fernández-Terán, R.; Zhang, L.; Fernandes, D. L. A.; Tian, L.; Chen, H.; Tian, H. Organic Polymer Dots as Photocatalysts

for Visible Light-Driven Hydrogen Generation. *Angew. Angew. Chem., Int. Ed.* **2016**, *55*, 12306−12310.

(50) Chang, S. Y.; Elewa, A. M.; Mohamed, M. G.; Mekhemer, I. M. A.; Samy, M. M.; Zhang, K.; Chou, H. H.; Kuo, S. W. Rational design and synthesis of bifunctional Dibenzo[g,p]chrysene-based conjugated microporous polymers for energy storage and visible light-driven photocatalytic hydrogen evolution. *Mater. Today. Chem.* **2023**, *33*, 101680.

(51) Wang, W. J.; Chen, K. H.; Yang, Z. W.; Peng, B. W.; He, L. N. Tuning of visible light-driven CO_2 reduction and hydrogen evolution activity by using POSS-modified porous organometallic polymers. *J. Mater. Chem. A* **2021**, *9*, 16699−16705.

(52) Mohamed, M. G.; Elsayed, M. H.; Ye, Y.; Samy, M. M.; Hassan, A. E.; Mansoure, T. H.; Wen, Z.; Chou, H. H.; Chen, K. H.; Kuo, S. W. Construction of Porous Organic/Inorganic Hybrid Polymers Based on Polyhedral Oligomeric Silsesquioxane for Energy Storage and Hydrogen Production from Water. *Polymers* **2023**, *15*, 182.

(53) Mohamed, M. G.; Samy, M. M.; Mansoure, T. H.; Li, C. J.; Li, W. C.; Chen, J. H.; Zhang, K.; Kuo, S. W. Microporous Carbon and Carbon/Metal Composite Materials Derived from Bio-Benzoxazine-Linked Precursor for CO_2 Capture and Energy Storage Applications. *Int. J. Mol. Sci.* **2022**, *23*, 347.

(54) Mohamed, M. G.; Sharma, S. U.; Yang, C.-H.; Samy, M. M.; Mohammed, A. A. K.; Chaganti, S. V.; Lee, J.-T.; Wei-Kuo, S. Anthraquinone-Enriched Conjugated Microporous Polymers as Organic Cathode Materials for High-Performance Lithium-Ion Batteries. *ACS Appl. Energy Mater.* **2021**, *4*, 14628−14639.

(55) Mohamed, M. G.; Chaganti, S. V.; Li, M. S.; Samy, M. M.; Sharma, S. U.; Lee, J. T.; Elsayed, M. H.; Chou, H. H.; Kuo, S. W. Ultrastable Porous Organic Polymers Containing Thianthrene and Pyrene Units as Organic Electrode Materials for Supercapacitors. *ACS Appl. Energy Mater.* **2022**, *5*, 6442−6452.

(56) Sharma, S. U.; Elsayed, M. H.; Mekhemer, I. M. A.; Meng, T. S.; Chou, H. H.; Kuo, S. W.; Mohamed, M. G. Rational design of pyrene and thienyltriazine-based conjugated microporous polymers for high-performance energy storage and visible-light photocatalytic hydrogen evolution from water. *Giant* **2024**, *17*, 100217.

(57) Mohamed, M. G.; Chen, C. C.; Zhang, K.; Kuo, S. W. Construction of three-dimensional porous organic polymers with enhanced CO_2 uptake performance via solid-state thermal conversion from tetrahedral benzoxazine-linked precursor. *Eur. Polym. J.* **2023**, *200*, 112551.

(58) Singh, P. N.; Mohamed, M. G.; Kuo, S. W. Systematic Design and Synthesis of Conjugated Microporous Polymers Containing Pyrene and Azobenzene Building Materials for High-Performance Energy Storage. *ACS Appl. Energy Mater.* **2023**, *6*, 11342−11351.

(59) Mohamed, M. G.; Chang, W. C.; Kuo, S. W. Crown Ether- and Benzoxazine-Linked Porous Organic Polymers Displaying Enhanced Metal Ion and CO_2 Capture through Solid-State Chemical Transformation. *Macromolecules* **2022**, *55*, 7879−7892.

(60) Mohamed, M. G.; Chaganti, S. V.; Sharma, S. U.; Samy, M. M.; Ejaz, M.; Lee, J. T.; Zhang, K.; Kuo, S. W. Constructing Conjugated Microporous Polymers Containing the Pyrene-4,5,9,10-Tetraone Unit for Energy Storage. *ACS Appl. Energy Mater.* **2022**, *5*, 10130−10140.

(61) Zhao, P.; Wang, L.; Wu, Y.; Yang, T.; Ding, Y.; Yang, H. G.; Hu, A. Hyperbranched Conjugated Polymer Dots: The Enhanced Photocatalytic Activity for Visible Light-Driven Hydrogen Production. *Macromolecules* **2019**, *52*, 4376−4384.

(62) Mohamed, M. G.; Elsayed, M. H.; Li, C. J.; Hassan, A. E.; Mekhemer, I. M. A.; Musa, A. F.; Hussien, M. K.; Chen, L. C.; Chen, K. H.; Chou, H. H.; Kuo, S. W. Reticular design and alkyne bridge engineering in donor-π-acceptor type conjugated microporous polymers for boosting photocatalytic hydrogen evolution. *J. Mater. Chem. A* **2024**, *12*, 7693−7710.

(63) Delley, B. From molecules to solids with the DMol3 approach. *J. Chem. Phys.* **2000**, *113*, 7756−7764.

(64) Zaier, R.; Ayachi, S. DFT molecular modeling studies of D-π-A-π-D type cyclopentadithiophene-diketopyrrolopyrrole based small molecules donor materials for organic photovoltaic cells. *Optik* **2021**, *239*, 166787.

(65) Biswas, S.; Pramanik, A.; Pal, S.; Sarkar, P. A theoretical perspective on the photovoltaic performance of S, N-heteroacenes: an even-odd effect on the charge separation dynamics. *J. Phys. Chem. C* **2017**, *121*, 2574−2587.

(66) Delgado-Montiel, T.; Baldenebro-López, J.; Soto-Rojo, R.; Glossman-Mitnik, D. Theoretical study of the effect of π-bridge on optical and electronic properties of carbazole-based sensitizers for DSSCs. *Molecules* **2020**, *25*, 3670.

(67) Martínez, J. Local reactivity descriptors from degenerate frontier molecular orbitals. *Chem. Phys. Lett.* **2009**, *478*, 310−322.

(68) Gázquez, J. L.; Cedillo, A.; Vela, A. Electrodonating and electroaccepting powers. *J. Phys. Chem. A* **2007**, *111*, 1966−1970.

(69) Adamo, C.; Jacquemin, D. The calculations of excited-state properties with Time-Dependent Density Functional Theory. *Chem. Soc. Rev.* **2013**, *42*, 845−856.

(70) Chen, W.; Wang, L.; Mo, D.; He, F.; Wen, Z.; Wu, X.; Xu, H.; Chen, L. Modulating benzothiadiazole-based covalent organic frameworks via halogenation for enhanced photocatalytic water splitting. *Angew. Chem., Int. Ed.* **2020**, *132*, 17050−17057.